The UK Infrared Telescope M33 monitoring project – II. The star formation history in the central square kiloparsec

Atefeh Javadi,[1,2]★ Jacco Th. van Loon[2] and Mohammad Taghi Mirtorabi[3]

[1]*School of Astronomy, Institute for Research in Fundamental Sciences (IPM), PO Box 19395-5531, Tehran, Iran*
[2]*Astrophysics Group, Lennard-Jones Laboratories, Keele University, Staffordshire ST5 5BG*
[3]*Physics Department, Alzahra University, Vanak, 1993891176, Tehran, Iran*

ABSTRACT

We have conducted a near-infrared monitoring campaign at the UK Infrared Telescope, of the Local Group spiral galaxy M33 (Triangulum). The main aim was to identify stars in the very final stage of their evolution, and for which the luminosity is more directly related to the birth mass than the more numerous less-evolved giant stars that continue to increase in luminosity. In this second paper of the series, we construct the birth mass function and hence derive the star formation history. The star formation rate has varied between ~ 0.002 and $0.007 \, M_{\odot} \, yr^{-1} \, kpc^{-2}$. We give evidence of two epochs of a star formation rate enhanced by a factor of a few – one that happened $\geq 6 \, Gyr$ ago and produced ≥ 80 per cent of the total mass in stars, and one around $250 \, Myr$ ago that lasted $\sim 200 \, Myr$ and formed ≤ 6 per cent of the mass in stars. We construct radial and azimuthal distributions in the image plane and in the galaxy plane for populations associated with old first-ascent red giant branch (RGB) stars, intermediate-age asymptotic giant branch (AGB) stars and young (massive) blue and red supergiants. We find that the RGB stars follow an spheroidal distribution, while younger stars follow a flat-disc distribution. The intermediate-age population displays signs of a pseudo-bulge or possibly a bar. The inner spiral arm pattern as recorded in mid-19th-century drawings is confirmed. We interpret our findings as evidence for an old, pressure-supported component and a younger disc formed 6 Gyr ago, with an accretion event occurring 250 Myr ago giving rise to the compact nucleus in M33. Our study provides support for recent Padova stellar evolution models except that super-AGB stars likely reach low temperatures and thus high mass-loss rates, supporting the super-AGB nature of the progenitors of dust-enshrouded supernovae such as SN 2008S.

Key words: stars: evolution – stars: luminosity function, mass function – galaxies: individual: M33 – galaxies: star formation – galaxies: stellar content – galaxies: structure.

1 INTRODUCTION

Spiral galaxies are among the more massive galaxies in the Universe, that in the Λ cold dark matter (ΛCDM) paradigm are believed to have formed from the agglomeration of smaller building blocks. They have gaseous, rotating discs, where spiral arms and rotational shear set the conditions within which star formation continues at a moderate rate in present times. In the central regions of spiral galaxies, more ellipsoidal, largely stellar and pressure-supported components exist – nuclear star clusters, bulges and 'bars', but the relative importance of these components varies among galaxies of this Hubble class. What determines the presence or absence of these structures, and indeed the spiral arm pattern itself, is not understood.

The Local Group galaxy Triangulum (Hodierna 1654) – hereafter referred to as M33 (Messier 1771) – offers us a unique opportunity to study a spiral galaxy up close, and in particular to learn more about the structure and evolution of the central regions of such galaxy, that in our own Milky Way are heavily obscured by the intervening dusty disc (van Loon et al. 2003; Benjamin et al. 2005). Our viewing angle with respect to the M33 disc is more favourable ($56°$–$57°$; Deul & van der Hulst 1987; Zaritsky, Elston & Hill 1989) than that of the larger M31 (Andromeda), whilst the distance to M33 is not much different from that to M31 ($\mu = 24.9$ mag; Bonanos et al. 2006). The stellar content of M33 was summarized beautifully in the review by van den Bergh (1991). The present-day star formation rate (SFR) in the central regions of M33 has been measured on the basis of optical photometry of massive main-sequence stars and Hα luminosity to be ~ 0.005–$0.1 \, M_{\odot} \, yr^{-1} \, kpc^{-2}$ (Wilson, Scoville & Rice 1991). Minniti, Olszewski & Rieke (1993) deduced from

★E-mail: atefeh@astro.keele.ac.uk

their infrared (IR) observations (in the *H* band at 1.6 μm) that a distinct star formation episode must have occurred in the 'bulge' of M33 within the last Gyr, unrelated to activity within the disc – they also showed that the bulge comprises also intermediate-age stars in contrast to the old, metal-poor halo of M33. The structure of the central region was investigated further at IR wavelengths by Regan & Vogel (1994) and Stephens & Frogel (2002); the central nucleus had been described in detail also by Lauer et al. (1998).

Galactic evolution is driven at the end points of stellar evolution, where copious mass loss returns chemically enriched and sometimes dusty matter back to the interstellar medium (ISM); the stellar winds of evolved stars and the violent deaths of the most massive stars also inject energy and momentum into the ISM, generating turbulence and galactic fountains when superbubbles pop as they reach the 'surface' of the galactic disc. The evolved stars are also excellent tracers, not just of the feedback processes, but also of the underlying populations, that were formed from millions to billions of years prior to their appearance. The evolved phases of evolution generally represent the most luminous, and often the coolest, making evolved stars brilliant beacons at IR wavelengths, where it is also easier to see them deep inside galaxies as dust is more transparent at those longer wavelengths than in the optical and ultraviolet where their main-sequence progenitors shine. The final stages of stellar evolution of stars with main-sequence masses up to $M \sim 30\,M_\odot$ – asymptotic giant branch (AGB) stars and red supergiants – are characterized by strong radial pulsations of the cool atmospheric layers, rendering them identifiable as long-period variables (LPVs) in photometric monitoring campaigns spanning months to years (e.g. Whitelock, Feast & Catchpole 1991; Wood 2000; Ita et al. 2004a,b).

The main objectives of the project are to construct the mass function of LPVs and derive from this the star formation history (SFH) in M33, to correlate spatial distributions of the LPVs of different mass with galactic structures (spheroid, disc and spiral arm components), to measure the rate at which dust is produced and fed into the ISM, to establish correlations between the dust production rate, luminosity and amplitude of an LPV and to compare the *in situ* dust replenishment with the amount of pre-existing dust (see Javadi, van Loon & Mirtorabi 2011b). This is Paper II in the series, describing the galactic structure and SFH in the inner square kpc. Paper I in the series presented the photometric catalogue of stars in the inner square kpc (Javadi, van Loon & Mirtorabi 2011a, hereafter Paper I). Subsequent papers in the series will discuss the mass-loss mechanism and dust production rate (Paper III), and the extension to a nearly square degree area covering much of the M33 optical disc (Paper IV).

2 THE INPUT DATA AND MODELS

In this section we briefly summarize the salient features of the catalogue of variable stars that we produced (Paper I), and of the stellar evolution models that we use here.

2.1 The catalogue of variable stars that we use

In Paper I we described the search for large-amplitude, long-period variable stars in the central 4×4 arcmin^2 (square kpc) of M33, with the UIST imager on the United Kingdom Infrared Telescope (UKIRT) on Mauna Kea, Hawaii. The monitoring was done predominantly in the *K* band (around a wavelength of $\lambda = 2.20\,\mu$m), with additional observations in the *J* and *H* bands ($\lambda = 1.28$ and 1.65 μm, respectively) mostly for the purpose of obtaining colour information. Observations were carried out if the near-IR stellar
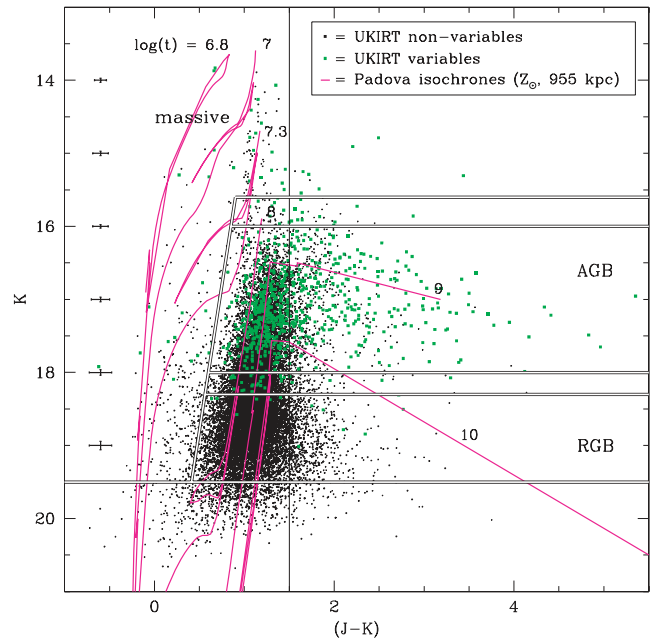

Figure 1. Colour–magnitude diagram of our UKIRT catalogue; variable stars are plotted in green. Representative photometric error bars are plotted. Overlain are isochrones (Marigo et al. 2008), labelled by their logarithmic ages – these include circumstellar reddening, showing up as large excursions towards red colours; carbonaceous dust (e.g. at $\log t = 9$) and oxygenous dust (e.g. at $\log t = 10$) have different reddening slopes. The vertical line at $J - K = 1.5$ mag indicates the colour criterion redwards of which a correction is applied for this reddening. The thick black-and-white lines demarcate the bulk of the populations of massive, AGB and RGB stars (separated by small buffers in *K*-band magnitude to avoid cross-contamination – see Section 4.2).

images were <0.8 arcsec. Each quadrant of the field was observed at least 11 times spread over the period 2003–2007, with stars in overlap regions being observed more often.

Photometry was obtained via fitting of the empirically derived point spread function to all stars detected above a threshold in terms of the local sky background noise. Hence a catalogue of 18 398 stars was produced. Fig. 1 shows these stars in a colour–magnitude diagram. The catalogue reaches a completeness level of >90 per cent above the RGB tip around $K \sim 18$ mag. For this bright magnitude regime, the photometric accuracy is <10 per cent, and blending is a concern in only ~1 per cent of cases. Contamination of the sample by stars in the Galactic foreground was demonstrated to be negligible.

The variability search was performed using the NEWTRIAL routine (Stetson 1993) on the basis of the '*L*' variability index (Stetson 1996), which includes an assessment of the variations in the measurements in comparison to the measurement uncertainties, both in terms of their ratio and distribution. Hence 812 variables were found, with estimated *K*-band amplitudes in the range $A_K \sim 0.2$–2 mag (typically $A_K \sim 0.6$ mag). Their distribution over magnitude and colour is shown in Fig. 1 (in green).

2.2 The stellar evolution models that we use

The best available theoretical models for our purpose are currently provided by the Padova group (Marigo et al. 2008) for the following reasons.

(i) They span an adequate range in birth mass ($0.8 < M < 30\,M_{\odot}$), combining their own models for intermediate-mass stars ($M < 7\,M_{\odot}$) with Padova models for more massive stars ($M > 7\,M_{\odot}$; Bertelli et al. 1994).

(ii) They are computed all the way through the thermal pulsing AGB until they enter the post-AGB phase, in a manner that is consistent with the computation of the preceding evolutionary stages. Crucially, it includes the third dredge-up mixing of the stellar mantle as a result of the helium-burning pulses, as well as the enhanced luminosity of massive AGB stars undergoing hot bottom burning (HBB; Iben & Renzini 1983).

(iii) They include molecular opacities that are important for the cool atmospheres of red giants, allowing to describe the transformation from oxygen-dominated M-type AGB stars to carbon stars in the approximate birth mass range $M \sim 1.5$–$4\,M_{\odot}$ (cf. Girardi & Marigo 2007).

(iv) They include predictions for dust production in the winds of LPVs and the associated reddening.

(v) They include predictions for the radial pulsation.

(vi) They have been carefully transformed to various optical and IR photometric systems.

(vii) They are available via a user-friendly internet interface.

We encourage other groups to apply the same principles to their models, so that their fundamental differences can be explored empirically to the greatest effect. While we refer to Marigo et al. (2008) and Marigo & Girardi (2007) for the technical details pertaining to their models, and we have no way of replacing them by different models, we point out a few essential aspects of this set of Padova models below.

The Padova models do not include the effects of rotation or magnetic fields on mixing within the stellar interior. Especially in massive stars these can have important consequences for their luminosities and lifetimes, making them brighter but live longer and evolve to cooler red supergiant stages (cf. Meynet & Maeder 2000; Heger, Woosley & Spruit 2005).

The Padova models employ convective overshoot (see Marigo & Girardi 2007), which prolongs the lifetime of a star. Hence stars of a given observed luminosity will be linked to older ages and lower birth masses than in other, classical models that do not allow for convective overshoot. This is mainly an issue for intermediate-age populations.

The thermal pulsing AGB is not computed by solving the equations governing the stellar internal structure, but in a synthetic way by adopting parametrizations which include the efficiency and threshold temperature at which third dredge-up sets in. These parameters have been calibrated empirically against observations, for instance, of the carbon star luminosity function and star clusters in the Magellanic Clouds (Marigo & Girardi 2007). Consequently, it is possible that these calibrations are not a perfect match to populations in galaxies other than the Magellanic Clouds. While stars in M33 are not vastly different from those in the Large Magellanic Cloud (LMC), stars in the nuclear region of M33 are probably more similar to solar-metallicity stars in the Milky Way.

More critically important is to note that the published isochrones do *not* include the excursions in luminosity and temperature resulting from the thermal pulses, but only record the evolution through the hydrogen-shell burning phases. While the latter dominates also on the TP-AGB, stars undergoing the thermal-pulse excursions may erroneously be assigned to lower or higher birth masses. This ultimately reduces the time resolution and contrast of the derived SFH somewhat.

The radial pulsation properties (period and mode) are computed as a function of luminosity. Stars are expected to start pulsating in the first overtone as soon as the thermal pulses start. The luminosity at which the transition to the fundamental mode occurs is based upon the linear pulsation models from Ostlie & Cox (1986), while periods are computed from the mass and radius based upon models from Fox & Wood (1982) – with some modifications to detail as described in Marigo & Girardi (2007, their section 2.7) and Marigo et al. (2008, their appendix). For the purpose of our work the main important feature is the lifetime of the pulsation phase, not so much the mode or period. The revisions made by Marigo et al. (2008) reduced the pulsation lifetime of the most massive AGB stars by a factor of 2–5, which in our analysis would lead to an increase in the associated SFR by the same amount (see Section 3.2).

Spectral templates used to describe the photospheric emission of the coolest giants come from empirical libraries for M-type stars (Fluks et al. 1994) or synthetic spectra for carbon stars (Loidl, Lançon & Jørgensen 2001). These may not always be entirely appropriate, for instance, at a different metallicity, carbon-to-oxygen ratio or dynamical state of the pulsating atmosphere. However, the uncertainty in the bolometric corrections is modest in the near-IR, likely <0.1 mag at K, and thus not a serious concern for our project.

Mass loss truncates the evolution of AGB stars, depleting their mantles and thereby avoiding the explosion of AGB stars of $M > 1.4\,M_{\odot}$. This becomes important when the mass-loss rates exceed the nuclear burning rate (van Loon et al. 1999). Mass loss also reduces the effective temperature and increases the pulsation period, as the less massive mantle inflates. Because all this happens quite suddenly, it is as important to accurately predict *when* this happens, as it is to accurately predict the *rate* of mass loss that is attained. The formalism adopted in the Padova models is based upon parametrization with respect to pulsation period (cf. Vassiliadis & Wood 1993). While this has observational support it does mean that the accuracy of the predicted mass loss relies critically on the model's accuracy with which it predicts the pulsation properties. Alternative prescriptions for mass loss exist that are defined in terms of luminosity and temperature (van Loon et al. 2005a). Mass loss is not as dramatic an issue for massive stars, which do explode before shedding their mantle through stellar mass loss, though mass loss could have an effect on the time these stars spend as a red supergiant.

Mass loss from cool stars also affects the photometric appearance of the star, as dust forming in the wind gives rise to selective extinction and thus diminishing brightness and reddening at optical/near-IR wavelengths. The effect at near-IR wavelengths only becomes noticeable in the case of very dense circumstellar envelopes. The Padova models incorporate these effects in a two-step procedure: (1) predict the radial density of the dust envelope, and (2) compute the resulting extinction of starlight at short wavelengths, and re-emission by the grains at long wavelengths. The first step is based mainly on the predictions from Ferrarotti & Gail (2006), whilst the second step follows standard radiative transfer computations as in Groenewegen (2006). The adopted wind structure and dust content have observational support (e.g. Marshall et al. 2004) but there can be many reasons for deviations from this standard, simplistic picture. Likewise, the optical properties of the grains that are adopted in the radiative transfer computations are reasonable (typical astronomical silicates or aluminium oxides for M-type stars and a mixture of amorphous carbon and silicate carbide for carbon stars) but not without uncertainties. For the purpose of the analysis presented here, the most important uncertainty is in the direction of the reddening vector in the near-IR colour–magnitude diagram. This is explored in some detail in Sections 3.1.1 and 4.1.1.

An important remaining uncertainty in the Padova models concerns the evolution of super-AGB stars, with birth masses $M \sim$ 5–10 $M_{\odot}$ (Siess 2007), which in their models are not computed all the way through the thermal pulsing phase and thus appear to terminate their evolution prematurely. We explore the consequences in this paper and offer some guidance to the models.

Fig. 1 includes several representative isochrones, which show good correspondence to the observed sequences of stars. The main regions in this diagram where massive stars, AGB stars and RGB stars are found are demarcated (see Section 4.2). Red AGB stars or massive stars, at $J - K > 1.5$ mag, are almost exclusively LPVs affected by *circumstellar* reddening; *interstellar* reddening was proven to be unimportant (see Paper I). The reddened stars form a minority among the sample of LPVs, but it is encouraging to see that the isochrones cover the regime of reddened LPVs fairly well.

3 FROM THE BRIGHTNESSES OF VARIABLE STARS TO A STAR FORMATION HISTORY

The SFH is described by the SFR, ξ, as a function of lapsed time, t. This function quantifies how many solar masses of gas are converted into stars per year, and we here express it per unit area projected on the sky. The combined mass of stars created between times t and $t + dt$ is

$$dM(t) = \xi(t)\,dt. \tag{1}$$

This corresponds to a number, N, of stars formed:

$$dN(t) = dM(t) \frac{\int_{min}^{max} f_{IMF}(m)\,dm}{\int_{min}^{max} f_{IMF}(m)m\,dm}, \tag{2}$$

where f_{IMF} is the initial mass function, defined by

$$f_{IMF} = Am^{-\alpha}, \tag{3}$$

where A is the normalization constant and α depends on the mass range, following Kroupa (2001):

$$\alpha = \begin{cases} +0.3 \pm 0.7 & \text{for} \quad \min \le m/M_{\odot} < 0.08, \\ +1.3 \pm 0.5 & \text{for} \quad 0.08 \le m/M_{\odot} < 0.50, \\ +2.3 \pm 0.3 & \text{for} \quad 0.50 \le m/M_{\odot} < \max. \end{cases} \tag{4}$$

The minimum and maximum of the stellar mass range are adopted to be 0.02 and 200 $M_{\odot}$, respectively. Reasonable changes in these values will result in changes in the SFR by hardly more than a factor of 2.

The question is how many of these stars, n, are variable stars around time t which is when we observe them. Suppose stars with mass between $m(t)$ and $m(t + dt)$ satisfy this condition, then the number of variable stars created between times t and $t + dt$ is

$$dn(t) = dN(t) \frac{\int_{m(t)}^{m(t+dt)} f_{IMF}(m)\,dm}{\int_{min}^{max} f_{IMF}(m)\,dm}. \tag{5}$$

Combining the above equations we have

$$dn(t) = \xi(t)\,dt \frac{\int_{m(t)}^{m(t+dt)} f_{IMF}(m)\,dm}{\int_{min}^{max} f_{IMF}(m)m\,dm}. \tag{6}$$

When we determine $\xi(t)$ over an age bin dt, the number of variable stars observed in that age bin, dn', depends on the duration of variability, δt, so

$$dn'(t) = dn(t) \frac{\delta t}{dt}. \tag{7}$$

Inverting the above equations we obtain a relation between the observed number of variable stars in a certain age bin, and the SFR that long ago:

$$\xi(t) = \frac{dn'(t)}{\delta t} \frac{\int_{min}^{max} f_{IMF}(m)m\,dm}{\int_{m(t)}^{m(t+dt)} f_{IMF}(m)\,dm}. \tag{8}$$

Note that the value of the normalization constant A in equation (3) does not matter here.

3.1 The relation between birth mass and K-band magnitude of large-amplitude variable stars

LPVs, which dominate the large-amplitude variables identified in our IR monitoring programme, have reached the very final stages of their evolution, and their brightness can thus be translated into their mass at birth by employing theoretical evolutionary tracks, or in this case just as well by isochrones. Inspection of the isochrones confirms that stars are at their brightest in the K band ($\lambda \sim 2\,\mu$m) when they also develop the pulsations that give rise to their large-amplitude variability.

Hence we constructed the mass–luminosity relation for the K band as depicted in Figs 2 (low- to intermediate-mass range) and 3 (which includes the most massive stars), for four different values of the overall metallicity, from supersolar – as in massive elliptical galaxies and subpopulations in the bulges of massive spiral galaxies such as the Milky Way – to subsolar values appropriate for the LMC and Small Magellanic Cloud (SMC). There are small but noticeable differences. The central region of M33 is characterized by approximately solar-metallicity ISM (Rosolowsky & Simon 2008; Magrini, Stanghellini & Villaver 2009) and young and intermediate-age stellar populations (Minniti et al. 1993; Massey et al. 1996), but also given that older stars will tend to have lower metallicities we err on the side of caution and adopt the $Z = 0.015$ result, which is either consistent with solar metallicity or slightly subsolar
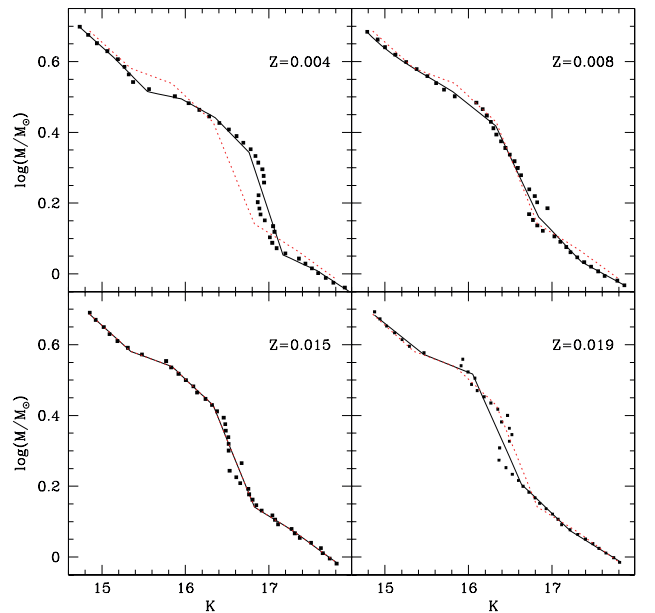

Figure 2. Mass–luminosity relation for $Z = 0.019$, 0.015, 0.008 and 0.004 for the K-band magnitude range corresponding to the low- to intermediate-mass range. Solid lines are the best linear spline fits, while the dotted lines are the fit for $Z = 0.015$ – which we apply for the variables stars of M33 galaxy – for comparison.
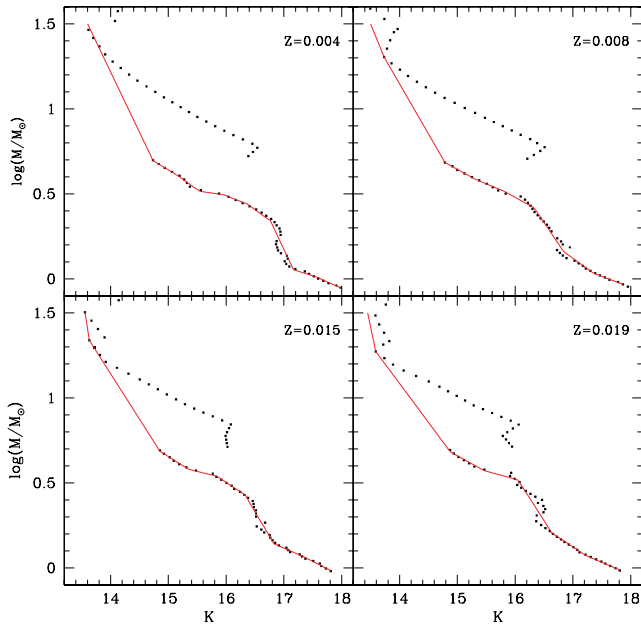
Figure 3. Mass–luminosity relation for $Z = 0.019$, 0.015, 0.008 and 0.004. This graph shows the relation for the full range of K-band magnitudes (dots). The solid lines are the linear spline fits for the case in which the function is interpolated across the super-AGB phase to massive red supergiants, i.e. for $0.7 < \log(M/M_\odot) < 1.2$–1.3.

metallicity depending on the exact metallicity adopted for the Sun ($Z = 0.015$ is close to the value for the Sun determined in recent years; cf. Asplund et al. 2009).

The mass–luminosity relations show small excursions in places, e.g. for $16 < K < 16.4$ mag at $Z = 0.019$, which could be related to differences in the bolometric corrections of M-type and carbon stars. However, some inaccuracies result from limited accuracy in the models as well as the time sampling of the evolutionary tracks and isochrones, and where there is doubt we interpolate over these small excursions by means of a spline fit, rendering a well-behaved function.

For $0.7 < \log(M/M_\odot) < 1.2$–1.3, the isochrones suggest an excursion towards fainter K-band magnitudes (Fig. 3), but as noted earlier the models were not computed through to the end of the evolution of these super-AGB stars (and possibly stars at the lower end of the mass range for red supergiants). In our analysis, we follow two different approaches, and investigate the impact on the derived SFH.

(1) We interpolate the mass–luminosity relation (and the mass–pulsation duration relation, see further) over this mass range to connect the final luminosities of AGB stars to those of massive red supergiants in a monotonic manner. Stars with $\log(M/M_\odot) > 1.5$ do not appear to become red supergiants and they are therefore not expected to exhibit periodic large-amplitude variability. This is our preferred solution, which we vindicate in Section 4.1.5.

(2) We accept the jump to fainter magnitudes from AGB to super-AGB stars. This is an extreme measure, as we believe super-AGB stars should reach high luminosities as they undergo HBB, though more massive red supergiants do not. We postpone following this choice to Section 4.1.5, where we show that it leads to physically unrealistic results.

The coefficients of the best-fitting function are obtained by minimization of χ^2 with the IRAF task NFIT1D except where it was deemed

Table 1. Mass–luminosity relation, $\log M\,[\mathrm{M_\odot}] = aK + b$, where K is the K-band magnitude on the Two Micron All Sky Survey (2MASS) system, for four values of metallicity, for the case in which the function is interpolated across the super-AGB phase to massive red supergiants.

a	b	Validity range
	$Z = 0.019$	
−1.627	23.3812	$K \leq 13.590$
−0.458	6.5002	$13.590 < K \leq 14.875$
−0.188 ± 0.053	3.492 ± 0.081	$14.875 < K \leq 15.462$
−0.094 ± 0.045	2.027 ± 0.071	$15.462 < K \leq 16.049$
−0.532 ± 0.033	9.049 ± 0.053	$16.049 < K \leq 16.635$
−0.225 ± 0.029	3.951 ± 0.045	$16.635 < K \leq 17.222$
−0.143 ± 0.041	2.541 ± 0.061	$K > 17.222$
	$Z = 0.015$	
−2.198	31.3051	$K \leq 13.633$
−0.535	8.6253	$13.633 < K \leq 14.854$
−0.213 ± 0.027	3.844 ± 0.040	$14.854 < K \leq 15.347$
−0.088 ± 0.018	1.924 ± 0.023	$15.347 < K \leq 15.840$
−0.222 ± 0.021	4.056 ± 0.024	$15.840 < K \leq 16.332$
−0.582 ± 0.012	9.937 ± 0.014	$16.332 < K \leq 16.825$
−0.147 ± 0.013	2.620 ± 0.016	$16.825 < K \leq 17.318$
−0.173 ± 0.022	3.060 ± 0.032	$K > 17.318$
	$Z = 0.008$	
−0.840	12.840	$K \leq 13.732$
−0.589	9.391	$13.732 < K \leq 14.787$
−0.188 ± 0.028	3.465 ± 0.043	$14.787 < K \leq 15.300$
−0.142 ± 0.027	2.758 ± 0.041	$15.300 < K \leq 15.813$
−0.188 ± 0.022	3.487 ± 0.036	$15.813 < K \leq 16.327$
−0.501 ± 0.016	8.183 ± 0.024	$16.327 < K \leq 16.840$
−0.248 ± 0.018	4.335 ± 0.026	$16.840 < K \leq 17.353$
−0.128 ± 0.025	2.257 ± 0.035	$K > 17.353$
	$Z = 0.004$	
−0.708	11.1268	$K \leq 14.734$
−0.209 ± 0.051	3.783 ± 0.077	$14.734 < K \leq 15.140$
−0.240 ± 0.054	4.244 ± 0.078	$15.140 < K \leq 15.545$
−0.050 ± 0.060	0.565 ± 0.091	$15.545 < K \leq 15.951$
−0.131 ± 0.054	2.583 ± 0.083	$15.951 < K \leq 16.356$
−0.243 ± 0.041	4.409 ± 0.057	$16.356 < K \leq 16.762$
−0.714 ± 0.039	12.310 ± 0.055	$16.762 < K \leq 17.167$
−0.109 ± 0.043	1.932 ± 0.070	$17.167 < K \leq 17.573$
−0.153 ± 0.046	2.690 ± 0.067	$K > 17.573$

more appropriate to be guided by two end points of isochrones, in which case no estimates of uncertainty are attached. For case (1) the function is described in Table 1.

3.1.1 Correction for extinction by dust

By determining the mass–luminosity relation we now can convert the K-band magnitudes of the variable stars to their masses, and derive the present-day mass function of variable stars. However, the K-band magnitude of a star seen through a high dust column density is diminished, and should be corrected to the value on the mass–luminosity relation. Although the isochrones of Marigo et al. (2008) include the effects of circumstellar dust formation, these are very uncertain and we prefer a simple de-reddening procedure. This would also naturally account for any additional interstellar

extinction, at least to some extent.[1] The de-reddening correction is related to the colour and magnitude of a star. In Fig. 1 we show the Marigo et al. (2008) isochrones for a range of ages. It immediately becomes clear that the reddening for carbon stars (e.g. at $t = 1$ Gyr, i.e. $\log t = 9$) differs from that of oxygen-rich stars (e.g. at $t = 10$ Gyr, i.e. $\log t = 10$), the former more quickly reddening compared to the extinction in the K band. The average slope of the reddening of carbon stars is 0.52 mag of K-band extinction per magnitude of $J - K$ reddening, whilst it is 0.72 mag mag^{-1} for oxygen-rich stars. The locus to which we translate the reddened star is at $J - K = 1.25$ mag, but we apply the correction to those variable stars that have $J - K > 1.5$ mag to allow some deviations from the unreddened locus as a result of photometric inaccuracies and variability. Hence the correction equation is

$$K_0 = K + a(1.25 - (J - K)). \tag{9}$$

If only K- and H-band data are available but no J-band data, then we apply the following correction derived from the K versus $H - K$ diagram:

$$K_0 = K + a(0.3 - (H - K)). \tag{10}$$

In the case where only K-band but neither J- nor H-band data are available, we adopt $J - K = 4$ mag (roughly equivalent to where we start losing stars too red for our survey depth), and use equation (9). The constants in these equations are $a = 1.06$ for carbon stars and $a = 1.6$ for oxygen-rich stars.[2]

It is thus important to know which stars have carbonaceous dust and which ones have oxygeneous dust. As described in Paper I, the only catalogue available that uses an identification technique based on specific spectral features is the one published by Rowe et al. (2005). Then, following the recommendation by those authors, we set limits on the photometric errors in their catalogue of <0.05 mag, resulting in just three variable carbon stars. This is insufficient to decide which red stars in our catalogue are likely to be carbon stars. Setting no limit on errors resulted in five variable carbon stars, of which three have $J - K > 1.5$ mag. However, we expect from theory and observations in the LMC (Groenewegen & de Jong 1993; van Loon, Marshall & Zijlstra 2005b; Girardi & Marigo 2007) that solar and slightly subsolar metallicity carbon stars arise from stars in a birth mass range of ≈ 1.5–$4\,M_\odot$: third dredge-up is not strong enough to turn lower mass AGB stars into carbon stars, while HBB prevents carbon to enrich the surface of more massive AGB stars. Hence we first apply the carbon-dust correction to all reddened stars – if the derived mass is in the 1.5–$4\,M_\odot$ range then we accept that star as a carbon star, else we apply the oxygeneous dust correction.

In Fig. 4 we show the resulting PMF for the variable stars in the central square kpc of M33. As indicated in Paper I, nine of the large-amplitude variable stars show indications of blending so we removed those stars from our analysis and we derive the SFH using the remaining 803 variables. We applied the dereddening correction as described above, as well as *only* a carbonaceous dust correction and *only* an oxygeneous dust correction: the differences are slight and mostly reflected in a ∼50 per cent scatter in the ∼$2\,M_\odot$ region.

---

[1] Interstellar dust will have somewhat different optical properties from those of circumstellar dust. Then again, interstellar extinction is not generally observed to be a major factor in this region of M33, whereas circumstellar dust is evident in a considerable fraction of the highly evolved AGB stars – see Paper I.

[2] In the remainder we assume all photometry has been corrected for extinction, and we do not explicitly use the subscript '0'.
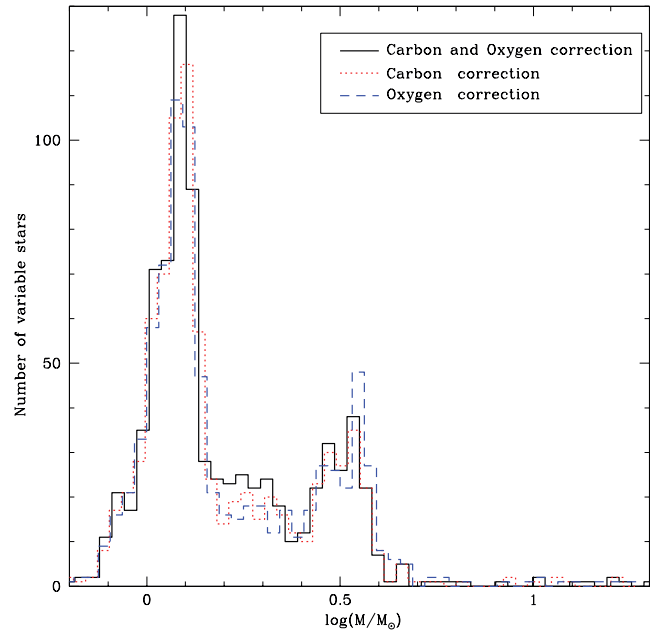
Figure 4. Present-day mass function of large-amplitude variable stars in the central square kpc of M33. The solid black line is the histogram obtained by applying the dereddening correction dependent on the mass of the star, the dotted red and dashed blue lines are the results obtained when applying *only* the carbonaceous dust correction or *only* the oxygeneous dust correction, respectively.

3.2 The mass-dependent duration of large-amplitude variability

Equation (1) contains a correction factor for the duration in which a star is seen to pulsate with large amplitude. For instance, massive stars evolve faster and are captured in their pulsating phase only briefly, whereas lower mass stars spend longer in that phase and are thus more likely and more numerous to appear in variability surveys – aside from the effects of the IMF, and of the SFH that we are after.

To derive this correction we followed the predictions from the Marigo et al. (2008) isochrones, so as to be consistent within our analysis. The isochrone tables indicate the phase of strong radial pulsation, and we take this entire duration as the time during which the star would have been identified in our survey (Paper I) as a variable star. We derived a function of mass for this duration of pulsation by fitting a multiple-Gaussian function to these isochrone values. As we investigate two cases – one in which we interpolate between the most massive AGB stars and the more massive red supergiants, and another in which we accept the regression in K-band brightness over the super-AGB star mass regime – we also take these two approaches with regard to the pulsation duration versus mass function (the mass–pulsation relation): if the super-AGB stars *do* evolve to higher luminosities and cooler temperatures then they will also be more likely to, and longer, pulsate.

Hence, for case (1) we fitted three Gaussian functions to the mass–pulsation diagram and interpolated over the same mass range as in the mass–luminosity diagram. The result is tabulated in Table 2 and shown in Fig. 5 (top panel). For case (2), we fit two independent sets of Gaussian functions – one for the low-mass stars and one for the high-mass stars (see Section 4.1.5).

Table 2. Mass–pulsation relation, $\log(\delta t/t) = D + \sum_{i=1}^{3} a_i \exp((\log M\,[\mathrm{M}_\odot] - b_i)^2/(2c_i^2))$, where δt is the pulsation duration and t the age of the star, for four values of metallicity, for the case in which the function is interpolated across the super-AGB phase to massive red supergiants.

D	i	a	b	c
		$Z = 0.019$		
-4.42	1	3.04	1.271	0.277
	2	0.74	0.510	0.068
	3	1.35	0.478	0.331
		$Z = 0.015$		
-3.63	1	2.18	1.238	0.238
	2	1.36	0.514	0.127
	3	0.30	0.228	0.084
		$Z = 0.008$		
-3.96	1	2.34	1.281	0.378
	2	1.32	0.460	0.165
	3	0.38	0.145	0.067
		$Z = 0.004$		
-4.00	1	2.29	1.217	0.408
	2	0.84	0.524	0.093
	3	0.87	0.206	0.088

3.3 From a mass distribution to a star formation rate as a function of time

Here we have all the relations required to calculate the SFR, except that we still need to relate the birth mass of a variable star we see now, to the time lapsed since its formation. This transformation is easily derived from the Marigo et al. (2008) isochrones. The mass–age relation is displayed in Fig. 6, in which the data points are derived from the isochrones and the solid line is a function we fit to the data (the coefficients of which are listed in Table 3).

Now we have got all the tools ready to derive the SFH. For each star, first we examine whether the star is reddened or not and if so, we add the dereddening correction using the mass-dependent coefficients. Then, by using the coefficients from Table 1 for $Z = 0.015$, we convert the K-band magnitude to the birth mass and by using Table 2 we estimate the pulsation duration, the inverse of which is the weight assigned to the star. We do this by interpolation across the super-AGB regime – later (in Section 4.1.5) we investigate the difference obtained by following the isochrones exactly. Then, we convert the birth mass to lapsed time (age). The only remaining correction to be applied is the IMF.

An important detail related to the presentation of a SFH is the way it is binned in age. The younger, massive variable stars are many times fewer than the old, low-mass variable stars and inadequate binning can either lead to spurious peaks in the SFR or mask any such real bursts. From a statistical point of view there is advantage is assuring that each bin contains the same number of stars, so the SFR values have uniform uncertainties. To accomplish this, we first ordered the stars by mass, then start counting until we reach a given number, at which moment we start counting stars for the subsequent bin. Eventually, the IMF correction is applied based on the minimum and maximum mass of each bin.
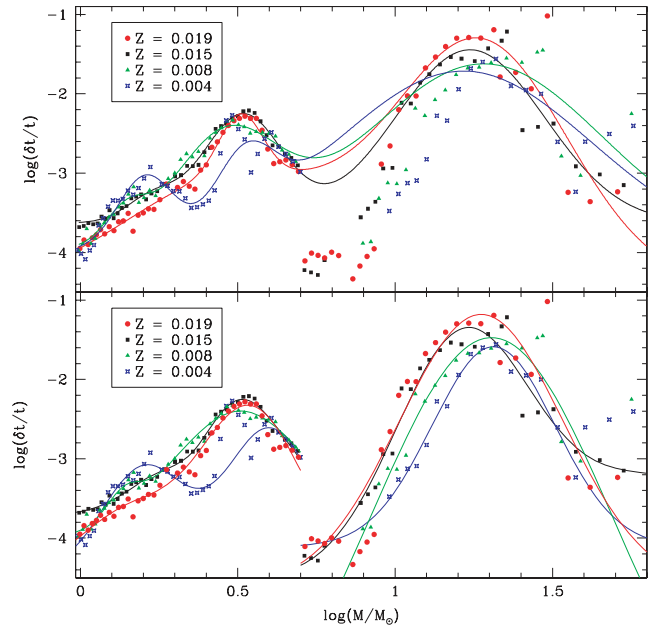

Figure 5. Mass–pulsation relation. The points show the ratio of pulsation duration to age as tabulated in the Marigo et al. (2008) isochrones; the solid lines are our multiple-Gaussian fits to these data: interpolating over the super-AGB regime (top panel, for four choices of metallicity Z) and accepting the jump in K-band brightness between the AGB and super-AGB (bottom panel).
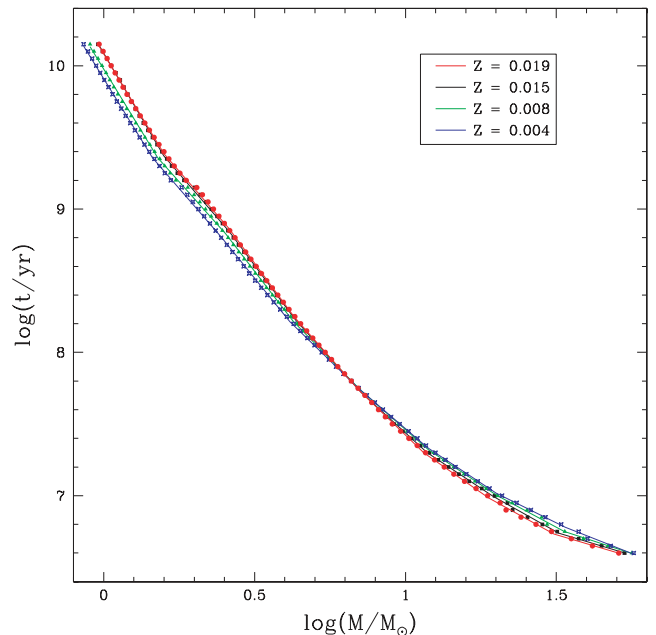

Figure 6. Birth: mass–age relation for AGB stars and red supergiants derived from the Marigo et al. (2008) isochrones for four choices of metallicity (dots, Z), along with linear spline fits.

4 THE STAR FORMATION HISTORY IN M33

The obtained SFH for the central square kpc of M33 is shown in Fig. 7. The horizontal 'error bars' correspond to the start and end time for which the SFR was calculated in that bin. The oldest bin is only shown in part as it extends to (unrealistically) large ages. The only reason it is plotted is to show that, as expected, the SFR
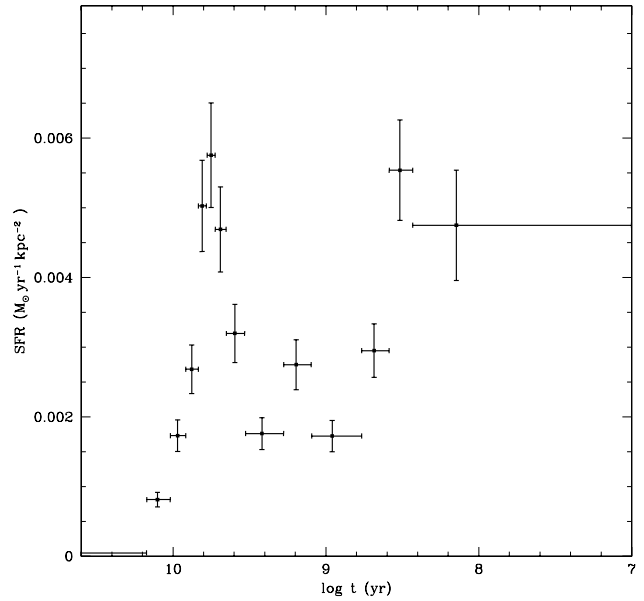
Table 3. Mass–age relation, $\log t \, [\mathrm{yr}] = a \log M \, [\mathrm{M}_\odot] + b$.

a	b	Validity range
	$Z = 0.019$	
-3.480 ± 0.008	10.082 ± 0.019	$\log M \leq 0.200$
-2.433 ± 0.007	9.873 ± 0.010	$0.200 < \log M \leq 0.415$
-2.866 ± 0.007	10.054 ± 0.010	$0.415 < \log M \leq 0.631$
-2.381 ± 0.007	9.750 ± 0.010	$0.631 < \log M \leq 0.846$
-2.027 ± 0.008	9.450 ± 0.012	$0.846 < \log M \leq 1.061$
-1.463 ± 0.009	8.852 ± 0.013	$1.061 < \log M \leq 1.277$
-1.168 ± 0.011	8.474 ± 0.016	$1.277 < \log M \leq 1.492$
-0.621 ± 0.014	7.600 ± 0.019	$\log M > 1.492$
	$Z = 0.015$	
-3.062 ± 0.007	10.096 ± 0.011	$\log M \leq 0.237$
-2.425 ± 0.007	9.945 ± 0.010	$0.237 < \log M \leq 0.455$
-2.824 ± 0.007	10.127 ± 0.010	$0.455 < \log M \leq 0.674$
-2.316 ± 0.007	9.786 ± 0.011	$0.674 < \log M \leq 0.892$
-1.926 ± 0.008	9.438 ± 0.012	$0.892 < \log M \leq 1.110$
-1.399 ± 0.009	8.853 ± 0.013	$1.110 < \log M \leq 1.328$
-1.180 ± 0.063	8.562 ± 0.067	$1.328 < \log M \leq 1.546$
-0.625 ± 0.013	7.704 ± 0.018	$\log M > 1.546$
	$Z = 0.008$	
-3.461 ± 0.008	9.976 ± 0.012	$\log M \leq 0.179$
-2.347 ± 0.007	9.776 ± 0.011	$0.179 < \log M \leq 0.404$
-2.727 ± 0.008	9.930 ± 0.011	$0.404 < \log M \leq 0.628$
-2.154 ± 0.008	9.570 ± 0.014	$0.628 < \log M \leq 0.853$
-1.848 ± 0.009	9.309 ± 0.015	$0.853 < \log M \leq 1.077$
-1.398 ± 0.010	8.825 ± 0.015	$1.077 < \log M \leq 1.302$
-1.134 ± 0.012	8.451 ± 0.017	$1.302 < \log M \leq 1.526$
-0.681 ± 0.015	7.790 ± 0.021	$\log M > 1.526$
	$Z = 0.004$	
-3.416 ± 0.007	9.910 ± 0.011	$\log M \leq 0.161$
-2.436 ± 0.007	9.752 ± 0.010	$0.161 < \log M \leq 0.389$
-2.588 ± 0.007	9.812 ± 0.011	$0.389 < \log M \leq 0.617$
-2.043 ± 0.007	9.475 ± 0.011	$0.617 < \log M \leq 0.845$
-1.812 ± 0.008	9.280 ± 0.012	$0.845 < \log M \leq 1.073$
-1.395 ± 0.010	8.832 ± 0.013	$1.073 < \log M \leq 1.301$
-1.036 ± 0.011	8.365 ± 0.016	$1.301 < \log M \leq 1.529$
-0.829 ± 0.014	8.048 ± 0.020	$\log M > 1.529$

Figure 7. The SFH in the central square kpc of M33 derived from near-IR AGB star and red-supergiant variables.

we estimate for ages exceeding the Hubble time is negligible. We prefer not to rescale the diagrams so as not to degrade their visibility in the ranges where it matters.

The SFH is characterized by a major epoch of formation ≈ 4–8 Gyr ago ($\log t = 9.6$–9.9), peaking around 6 Gyr ago ($\log t = 9.8$) at a level about three times as high as during the subsequent couple of Gyr. This corroborates the result obtained by Cioni et al. (2008) that the nuclear region of M33 is on average nearly as old as the outer disc, which they found to have an age of ~ 6 Gyr. The peak at 6 Gyr may not be real, though the mass–pulsation relation suggests that low-mass stars do not pulsate much. While this is only true in a relative sense (as they live long), the exact level and duration of pulsation for those stars may be somewhat uncertain. The SFR may thus well have been as high, or higher earlier than 6 Gyr ago. We are confident, though, that the SFR has dropped significantly since 5 Gyr ago ($\log t < 9.7$).

A more recent epoch of enhanced star formation is seen too, occurring ~ 200–300 Myr ago ($\log t = 8.3$–8.5), nearly reaching the same level as the 6-Gyr peak ($\log t = 9.8$). Since then the rate of star

formation appears to have diminished again. This would confirm the early recognition by Minniti et al. (1993) of a substantial star formation episode in the 'bulge' of M33 within the past Gyr ($\log t < 9$). It would be difficult to reliably recover such short-duration enhancements in SFR at intermediate ages more than a Gyr ago. For instance the higher bin around 1.5 Gyr ago ($\log t = 9.2$) might well correspond to such period of enhanced star formation, but on the basis of the star number statistics (represented by the vertical error bars in Fig. 7) we must conclude that such assertion would be unfounded.

The present-day SFR in the inner disc of M33 (over a $4 \, \mathrm{kpc}^2$ area) has been estimated by Wilson et al. (1991) on the basis of Hα and far-IR emission at $\xi = 0.01 \, \mathrm{M}_\odot \, \mathrm{yr}^{-1} \, \mathrm{kpc}^{-2}$. At $\xi = 0.0056 \pm 0.0008 \, \mathrm{M}_\odot \, \mathrm{yr}^{-1} \, \mathrm{kpc}^{-2}$ both the ancient and recent epochs of enhanced star formation that we have identified appear to be similar in intensity to the estimates by Wilson et al. Theirs are valid for the most recent few 10^7 yr, however. In our sample of variable stars we count six stars with ages $t < 20 \, \mathrm{Myr}$ ($\log t < 7.3$, birth masses $> 12 \, \mathrm{M}_\odot$). The SFR derived from this recently formed population is $\xi = 0.007 \pm 0.003 \, \mathrm{M}_\odot \, \mathrm{yr}^{-1} \, \mathrm{kpc}^{-2}$; while the error bar on this value is rather large, the value is in excellent agreement with the value derived by Wilson et al. on the basis of a very different method. This is very reassuring, and to a certain degree validates our methodology.

Based on our SFH, the total mass in stars formed over the history of M33 amounts to $3.9 \times 10^7 \, \mathrm{M}_\odot \, \mathrm{kpc}^{-2}$, of which $3.1 \times 10^7 \, \mathrm{M}_\odot \, \mathrm{kpc}^{-2}$ (or 80 per cent) was formed at ages $t > 4 \, \mathrm{Gyr}$ ($\log t > 9.6$). In contrast, the most recent epoch of enhanced star formation, at $t < 500 \, \mathrm{Myr}$ ($\log t < 8.7$), has only produced $2.4 \times 10^6 \, \mathrm{M}_\odot \, \mathrm{kpc}^{-2}$ (or 6 per cent). These estimates assume that there has not been a net migration into or out of the central square kpc region that we have monitored. Especially for the older stars this may not be true, and they could have preferentially migrated out of the central region as a result of dynamical relaxation (cf. van Loon et al. 2003). So the SFR – and total stellar mass formed – that we derive for ages $t \gtrsim 5 \, \mathrm{Gyr}$ ($\log t \gtrsim 9.7$) may have been underestimated.

Long, Charles & Dubus (2002) determined that the nucleus (central few arcsec) of M33 underwent two discrete epochs of star

formation, one a Gyr ago ($\log t = 9$) which formed 4 per cent of the $2 \times 10^6\,\mathrm{M}_\odot$ in stellar mass in the nuclear star cluster (cf. Kormendy & McClure 1993), and another only $\sim 40\,\mathrm{Myr}$ ago ($\log t \sim 7.6$) which added just half a per cent to the cluster's mass. Curiously, while timed differently (though with a degree of uncertainty), this resembles the increment in stellar mass (6 per cent) that we found to have formed within the past 0.5 Gyr ($\log t < 8.7$) in the surrounding central disc. At the SFR that we derived for the past 20 Myr ($\log t < 7.3$), the most recent of the two star formation events in the nucleus would have lasted approximately 1 Myr ($\log \Delta t = 6$), which is a typical time-scale for star cluster formation. These comparisons are suggestive of some connection between the nucleus and surrounding disc, and possibly of a more similar timing of events.

4.1 Variation in assumptions

In this section we examine how the derived SFH changes if we change our assumptions: the selection or omission of reddened stars, the amplitude threshold, the distance modulus and the treatment of the super-AGB stars.

4.1.1 Reddened stars

We can examine the contribution of the reddened stars to the SFH that we derive from the large-amplitude variables. Our catalogue of variable stars in the central square kpc of M33 contains 318 stars that have $J - K > 1.5\,\mathrm{mag}$ (but one of these is removed because it was affected by blending), which corresponds to the significant fraction of 39 per cent of all variable stars. These stars need a correction to their K-band magnitudes. Much redder stars, though rarer, may have been missed entirely by less IR-sensitive surveys. Of all reddened stars, 45 per cent were identified as variable. Of the remaining 55 per cent, some might well also be variable stars not identified as such in our survey, though it is likely that some fraction of this concerns non-variable stars seen behind interstellar dust clouds.

Fig. 8 shows the SFH we derive based solely on reddened ($J - K > 1.5\,\mathrm{mag}$) variable stars identified in our survey. As before, a mass-dependent dereddening correction has been applied to account for a mixture of carbon and oxygen-rich stars. Two things stand out immediately: the major historical star formation epoch at 4–10 Gyr ($\log t = 9.6$–10) disappeared and also the SFR in the most recent 250 Myr ($\log t < 8.4$) has dropped. On the other hand, reddened stars dominate the variable stars associated with the SFR derived at intermediate ages, 0.25–2.5 Gyr ago ($\log t < 8.4$–9.4). Most of these are expected to be carbon stars. Clearly, massive and low-mass stars do not feature prominently among the reddened stars. We argue, as we did in Paper I, that the low-mass stars may become very red (and thus be missed even by our IR survey) but possibly only very late in their pulsating phase, whilst massive stars do not envelope themselves in optically thick dust envelopes except in the most extreme, and thus rare cases (cf. van Loon et al. 1997). In conclusion, to obtain a complete SFH based on variable stars one must account for reddened stars so as to not underestimate the SFR at intermediate ages, while the earliest and most recent SFR is determined by optically bright(er) variable stars.

Our decision to only correct for reddening stars with $J - K > 1.5\,\mathrm{mag}$, and to correct them to a locus of $J - K = 1.25\,\mathrm{mag}$, may introduce some uncertainty. If either choice were made differently, the corrected brightness and hence inferred birth mass and thus age would be different. We had introduced the 0.25 mag 'buffer'
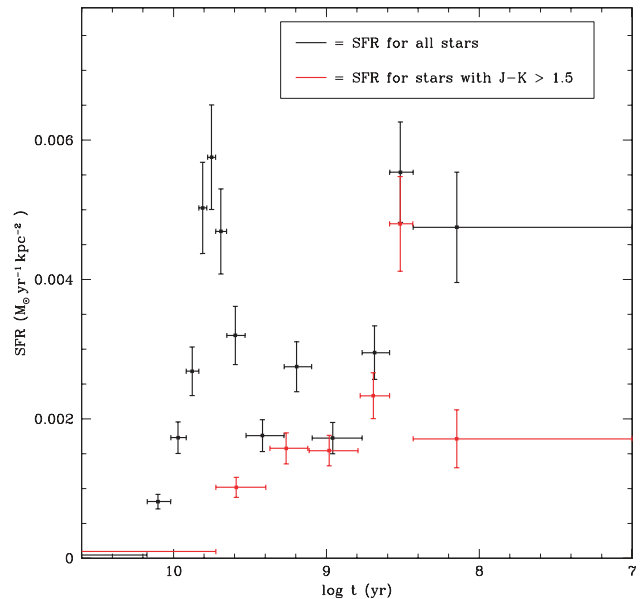

Figure 8. Contribution to the derived SFH by reddened variable stars with $J - K > 1.5\,\mathrm{mag}$ (in red), compared to the original result (in black).

between the locus of unreddened stars and the threshold for correcting for reddening to allow for photometric uncertainty which if corrected as if it were due to reddening would lead to systematic deviations. The photometric uncertainty in the colour is typically $\sim 0.1\,\mathrm{mag}$ (Fig. 1). The amplitudes of variability are typically 0.6 mag; while the colours vary less, with only a few measurements in the bands other than the K band the time-average colours may be inaccurate by a few tenths of a magnitude. This, and the morphology in the colour–magnitude diagram (Fig. 1), supports a $J - K > 1.5\,\mathrm{mag}$ threshold. One could argue for a shift of this, or of the unreddened locus, by 0.1 mag or so, but this would only lead to a shift (largely systematic) in unreddened K-band brightness by a similar magnitude. This would resemble varying the distance modulus by such amount. In Section 4.1.3 we investigate such shift but by as much as 0.4 mag. The effect of a 0.1 mag adjustment appears to be of little significance.

4.1.2 Amplitude threshold

How sensitive is the derived SFH to the exact threshold of our survey to the detection of variability? To gain some idea of this effect, we set a selection threshold on the estimated K-band amplitude (cf. Paper I) of $A_K > 0.5\,\mathrm{mag}$. This leaves us with 581 variable stars (excluding nine stars affected by blending – see Paper I), still nearly 3/4 of the original selection. It is likely that more stars were removed that have either low or high mass, as the former may not pulsate as vigorously (McDonald et al. 2010) while the latter do but not in terms of magnitude – which is a relative quantity, in relation to their high luminosity (cf. van Loon et al. 2008).

Fig. 9 shows the resulting SFH. The overall trend is little affected. Apart from an overall modest drop in the SFR, the effect seems to affect mostly the massive stars formed in the past 400 Myr ($\log t < 8.6$). The smaller amplitudes of low-mass stars is not apparent, but our SFH also does not extend into the past as far as the ages of old Galactic globular clusters ($t > 10\,\mathrm{Gyr}$, i.e. $\log t > 10$) upon which the evidence for diminished pulsation in low-mass red giants is largely based.
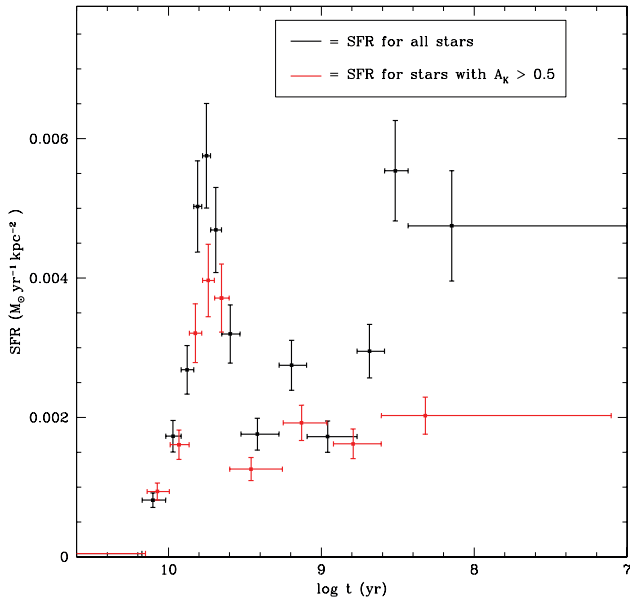
Figure 9. SFH derived after imposing a higher threshold on the estimated amplitude of variability, $A_K > 0.5$ mag (in red), compared to the original result (in black).

4.1.3 Distance modulus

In our analysis we adopted a distance modulus of $\mu = 24.9$ mag, which is found by several authors via different methods including eclipsing binaries, and which was found to match the theoretical isochrones quite well to our IR colour–magnitude diagrams. However, some authors have found lower values for the distance modulus, around $\mu = 24.5$ mag (Scowcroft et al. 2009). Changing the distance modulus will change the absolute magnitude of stars and hence also the mass of stars, but the mass–pulsation relation will remain unchanged as it does not depend on distance. This means that changing the distance modulus will affect the SFH we derive.

Fig. 10 shows the SFH for $\mu = 24.9$ (as before) and 24.5 mag. Overall the SFH has a similar behaviour despite the 20 per cent
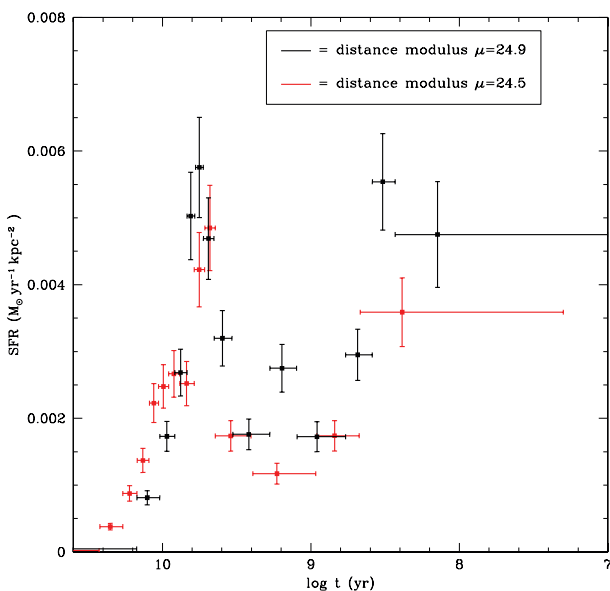
difference in distance, with a major ancient epoch of star formation and enhanced star formation in recent times. However, not surprisingly, the SFH is shifted towards earlier epochs. The SFR seems to be diminished at all later times; this is caused by the same effect, stars having been shifted to earlier times, piling up at ages $t \sim$ 10 Gyr ($\log t \sim 10$).

4.1.4 Metallicity

While the metallicity of the pulsating red giants in the centre of M33 is quite reliably known, the oldest pulsating stars might be somewhat deficient in metals compared to the young and intermediate-age $Z = 0.015$ population that formed after the initial period of star formation from which most chemical enrichment resulted. Investigating the metallicity dependence of our results also lays the foundation for the application of the method to the outskirts of the M33 disc, or to altogether different galaxies.

The parametrizations of the mass–luminosity relation (Figs 2 and 3; Table 1), mass–pulsation relation (Fig. 5, top; Table 2) and mass–age relation (Fig. 6; Table 3) have all been determined for four different values of the metallicity: $Z = 0.004$ (appropriate for the SMC), $Z = 0.008$ (appropriate for the LMC), $Z = 0.015$ (appropriate for the centre of M33) and $Z = 0.019$ (supersolar). The resulting SFHs are shown in Fig. 11.

The result from adopting $Z = 0.008$ hardly differs from the one we obtained for $Z = 0.015$. Apart from pushing the early epoch of star formation back by 1 or 2 Gyr there are no important deviations outside a $\sim$20 per cent margin. Adopting $Z = 0.019$ mainly extends the early epoch of star formation to as recent as 2 Gyr ago ($\log t = 9.3$) – the SFR would become fairly constant over the entire history of M33 except for a lull in activity $\sim$0.4–2 Gyr ago ($\log t = 8.6$–9.3). This strange result can be dismissed as such high metallicity is an unrealistic choice for M33. Adopting $Z = 0.004$ yields a 'burst' of star formation 0.2–1 Gyr ago ($\log t = 8.3$–9); whilst not impossible this is attributable to the shorter duration of pulsation predicted by the models (Fig. 5) for the birth mass range of 2–4 $M_\odot$ ($\log M = 0.3$–0.6; these are carbon stars) in combination with

Figure 10. SFH compared for two choices of the distance modulus: $\mu = 24.9$ (black) and 24.5 mag (red).
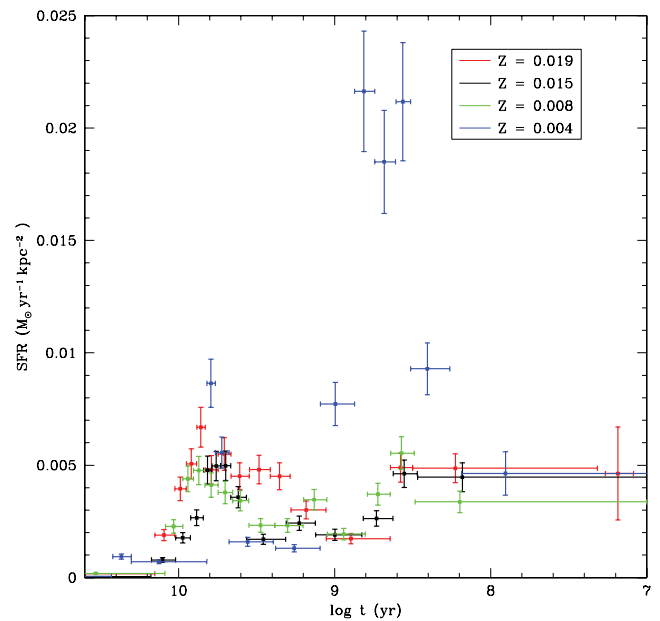

Figure 11. SFH compared for four choices of metallicity: $Z = 0.004$ (blue), 0.008 (green), 0.015 (black, appropriate for the M33 core) and 0.019 (red).
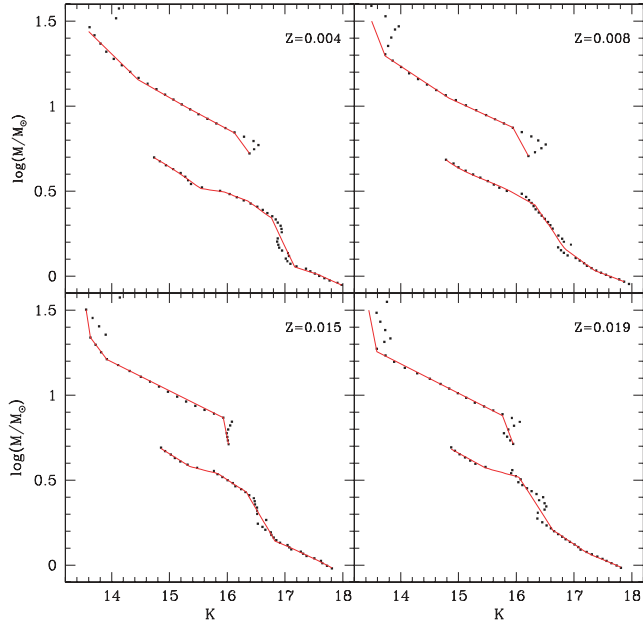
Figure 12. Mass–luminosity relation as in Fig. 3 but with the revised parametrization for the super-AGB stars and low-mass red supergiants. The solid lines are linear spline fits, requiring monotony everywhere except for the discontinuity at $\log(M/M_\odot) = 0.7$.

the observed high numbers of pulsating stars in that mass range. This low metallicity is not characteristic of the M33 population. In conclusion, the results we have derived by adopting $Z = 0.015$ are robust against reasonable deviations from this value for the metallicity.

4.1.5 Super-AGB stars

Previously, we have interpolated the mass–luminosity and mass–pulsation relations across the super-AGB and low-mass red supergiant regime, as the theoretical models had not been computed until the very end of these stars' evolution and we may thus have missed the coolest, strongly pulsating phases that these stars experience before ending their lives. Here, we examine how our results change if we do take the endpoints of the theoretical isochrones at face value.

Fig. 12 shows the revised mass–luminosity relation: the AGB portion, at $\log(M/M_\odot) < 0.7$, remains unchanged but the description of the more massive portion has been altered to follow the isochrones more closely (Table 4). We still keep that portion in itself monotonic, for simplicity. The small ranges where the slope has the opposite sign will not make a very different contribution because of this. Clearly, however, stars of $K \sim 15$ mag have two solutions for the mass, and we will need to devise some procedure to distribute the stars over these two solutions.

In the overlap region, we let us be guided by the IMF as to the relative fractions of the star that are to be assigned to the low- and high-mass solutions, respectively:

$$p_{low} = \int_{m_1}^{m_2} f_{IMF}\, dm, \tag{11}$$

$$p_{high} = \int_{m_1'}^{m_2'} f_{IMF}\, dm. \tag{12}$$

Table 4. Mass–luminosity relation, $\log M\,[M_\odot] = aK + b$, where K is the K-band magnitude on the 2MASS system, for four values of metallicity, for the case in which the end points of the isochrones covering the super-AGB phase have been taken at face value. Only the high-mass portion is given here – the low-mass portion remains as in Table 1.

a	b	Validity range
	$Z = 0.019$	
-1.749	25.034	$K \leq 13.590$
-0.173	3.609	$13.590 < K \leq 15.762$
-0.889	14.893	$15.762 < K \leq 15.948$
	$Z = 0.015$	
-2.198	31.305	$K \leq 13.633$
-0.451	7.491	$13.633 < K \leq 13.917$
-0.170	3.582	$13.917 < K \leq 15.930$
-1.673	17.311	$15.930 < K \leq 16.023$
	$Z = 0.008$	
-0.888	13.486	$K \leq 13.732$
-0.223 ± 0.004	4.355 ± 0.008	$13.732 < K \leq 14.837$
-0.157 ± 0.006	3.378 ± 0.009	$14.837 < K \leq 15.942$
-0.623 ± 0.003	10.811 ± 0.006	$15.942 < K \leq 16.211$
	$Z = 0.004$	
-0.272 ± 0.012	5.148 ± 0.018	$K \leq 14.453$
-0.681 ± 0.012	11.005 ± 0.018	$14.453 < K \leq 15.288$
-0.183 ± 0.013	3.801 ± 0.019	$15.288 < K \leq 16.124$
-0.458 ± 0.007	8.222 ± 0.014	$16.124 < K \leq 16.386$

Here, m_1 and m_2 are the masses calculated using the low-mass solution for each star, between $K - \delta K$ and $K + \delta K$, where δK is the error on the K-band magnitude; likewise, m_1' and m_2' delimit the high-mass range. Hence we obtain the normalized probabilities for the low- and high-mass solutions as follows:

$$P_{low} = \frac{p_{low}}{p_{low} + p_{high}}, \tag{13}$$

$$P_{high} = \frac{p_{high}}{p_{low} + p_{high}}, \tag{14}$$

so that each star still has unit weight, $P_{low} + P_{high} = 1$.

The remaining procedure follows that described above, but using the modified mass–pulsation relation given in Table 5 and displayed in Fig. 5. The resulting SFH is shown in Fig. 13.

In the overlap region we notice a sudden increase in the SFR, to ~20 times larger than the levels derived by interpolation. Such extreme behaviour right where the modification is made is highly implausible. Could it result from the implicit assumption that the SFR was the same for both solutions for the star's mass, underlying the formulae for the fractions p_{low} and p_{high}? The inflated values for the SFR are due to the high-mass branch of the dual solution. If the SFR in reality declined with time, then smaller fractions of stars ought to be assigned to that solution and the SFR would come down. However, the SFR must decline precipitously in order for the high-mass branch to be depleted, essentially resulting in fewer than one star to be observed in that regime. This would be very coincidental and thus also highly unlikely. Rather, we find it more likely that the high values for the SFR result from unrealistically brief adopted durations for their variability, δt (cf. Fig. 5).

We note that the oldest of the three age bins in the overlap region (at $\log t \sim 8.4$) now has a somewhat reduced SFR: this is because

Table 5. Mass–pulsation relation, $\log(\delta t/t) = D + \sum_{i=1}^{3} a_i \exp((\log M\,[\mathrm{M_\odot}] - b_i)^2/(2c_i^2))$, where δt is the pulsation duration and t the age of the star, for four values of metallicity, for the case in which the end points of the isochrones covering the super-AGB phase have been taken at face value.

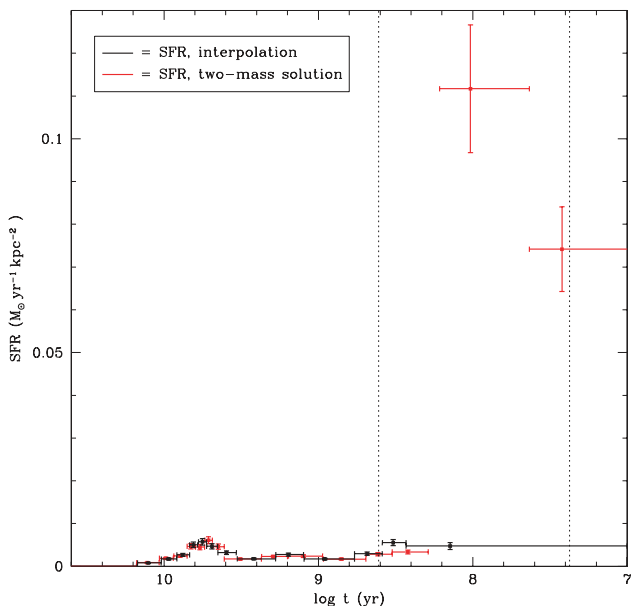| D	i	a_i	b_i	c_i	Validity range
			$Z = 0.019$		
−4.63	1	3.45	1.273	0.262	$\log M > 0.68$
	2	0.27	0.611	0.016	$\log M > 0.68$
−4.45	1	2.10	0.538	0.166	$\log M \le 0.68$
	2	0.75	0.149	0.153	$\log M \le 0.68$
			$Z = 0.015$		
−4.52	1	1.28	1.840	0.362	$\log M > 0.68$
	2	2.88	1.211	0.215	$\log M > 0.68$
−3.72	1	1.63	0.468	0.180	$\log M \le 0.68$
	2	−0.53	0.361	0.085	$\log M \le 0.68$
			$Z = 0.008$		
−7.13	1	5.66	1.306	0.381	$\log M > 0.68$
−4.02	1	1.62	0.509	0.217	$\log M \le 0.68$
	2	0.30	0.137	0.054	$\log M \le 0.68$
			$Z = 0.004$		
−4.11	1	2.52	1.313	0.195	$\log M > 0.68$
−4.44	1	1.82	0.602	0.142	$\log M \le 0.68$
	2	1.33	0.202	0.132	$\log M \le 0.68$

Figure 13. SFH for $Z = 0.015$, derived by assigning stars to dual solutions for their mass (in red), compared to the original result (in black); the vertical dotted lines indicate the extent of the overlap region.

these stars have been partly assigned to the high-mass branch of the solution whereas in the interpolated case they were all assigned to the low-mass branch of the solution. This is not odd in itself.

Thus we conclude that consistent use of the isochrones throughout the super-AGB and low-mass red supergiants regime leads to erroneous results. Thereby validating our interpolation of the mass–luminosity and mass–pulsation relations assuming that those

stars do become cooler and more luminous (cf. Ritossa, García-Berro & Iben 1996; Siess 2010) and that they do pulsate over longer durations than suggested by the isochrones (cf. Ventura & D'Antona 2011). As a consequence, we expect super-AGB stars to develop strong, dusty winds (following the mass-loss prescription of van Loon et al. 2005a). This lends support to the suggestion by Botticella et al. (2009) that the dust-enshrouded progenitor of SN 2008S was a super-AGB star.

We remind the reader that while the super-AGB stars undergo HBB and thus reach higher luminosities than calculated in the isochrones, red supergiants do not experience HBB and it is therefore not obvious that their evolution was also foreshortened in the calculation of the isochrones. The exact mass range of super-AGB stars is uncertain and could extend up to as high as $\sim 11\,\mathrm{M_\odot}$ if convective overshoot is ineffective (Eldridge & Tout 2004).

4.2 Spatial variations

Up till now, we have considered the SFH derived from the entire central square kpc ($4 \times 4\,\mathrm{arcmin^2}$) of M33. However, this region may well show different galactic structures associated with populations of stars formed at different times. Fig. 1 in Paper I clearly shows a central concentration of stars giving the appearance of a 'bulge' of $\sim$1-arcmin diameter. To examine this, first we define a circular region of radius $R = 110$ arcsec to avoid problems caused by the corners of the rectangular area covered in our UIST monitoring survey. Secondly, we separate the stars in our catalogue into massive stars, AGB stars and RGB stars, on the basis of K-band magnitude and $J - K$ colour criteria (see Fig. 1): we define a demarcation line between hot massive stars and cooler, less massive giant stars to run from $(J - K, K) = (0.6, 18)$ to $(J - K, K) = (0.9, 15.6)$ mag, with massive stars those that have $J - K$ colours bluer than this (down to $K = 19.5$ mag) or that have $K < 15.6$ mag, and AGB stars and RGB stars those that have $J - K$ colours redder than this and that have $16 < K < 18$ mag (AGB) or $18.3 < K < 19.5$ mag (RGB, which does extend to much fainter magnitudes than our survey completeness). We left small gaps to avoid contamination.

We consider two types of galactic structures: disc related and spheroidal. The former have axisymmetry in the galaxy plane and are otherwise 'flat' (with relatively little depth), while the latter have a surface density that is invariant to inclination with respect to the plane of the sky (as long as internal extinction is negligible, which we have shown in Paper I is largely the case for our near-IR survey). To investigate the disc-related structures, we must deproject the positions of stars on the image to the galaxy plane – but for the spheroidal structures we must make sure *not* to do that. To deproject, we first rotate the image according to the position angle (PA) = 23° and then stretch the coordinates along the direction of inclination according to an inclination angle of $i = 56°$ (Zaritsky et al. 1989).

The radial distributions of stars as measured in the galaxy plane are shown in Fig. 14. These are fitted with an adaptation for the stellar number density of the surface brightness function from Sérsic (1963):

$$N(r) = N_0 \exp(-b_n(r/R_e)^{1/n} - 1), \tag{15}$$

where $n = 4$ returns the de Vaucouleurs' profile typical of galaxy bulges (de Vaucouleurs 1953) and $n = 1$ an exponential disc. The calibration of the Sérsic profile is such that half the intensity (number of stars in our case) falls within $r = R_e$. The parameter b_n can be derived exactly from comparison of the complete and incomplete Gamma functions (Ciotti 1991), and approximately from
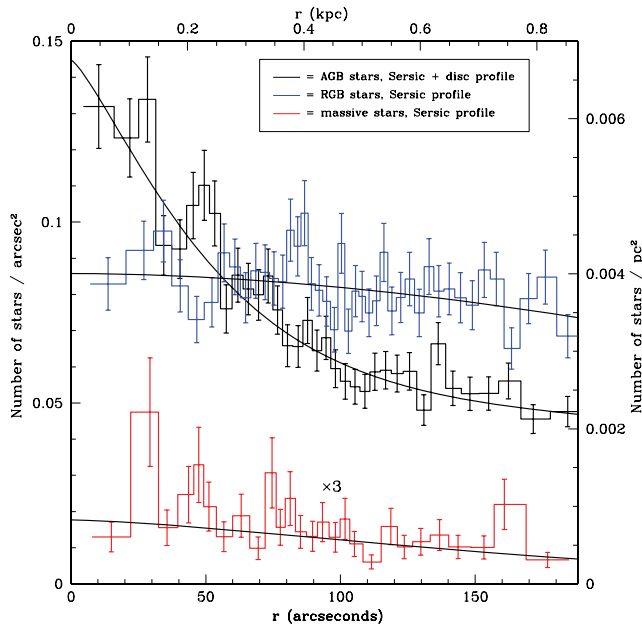
Figure 14. Radial distributions of massive stars (in red, multiplied by 3 for ease of comparison), AGB stars (in black) and RGB stars (in blue) in the galaxy plane. Each of these is fitted with a Sérsic profile (the fit parameters are listed in Table 6).
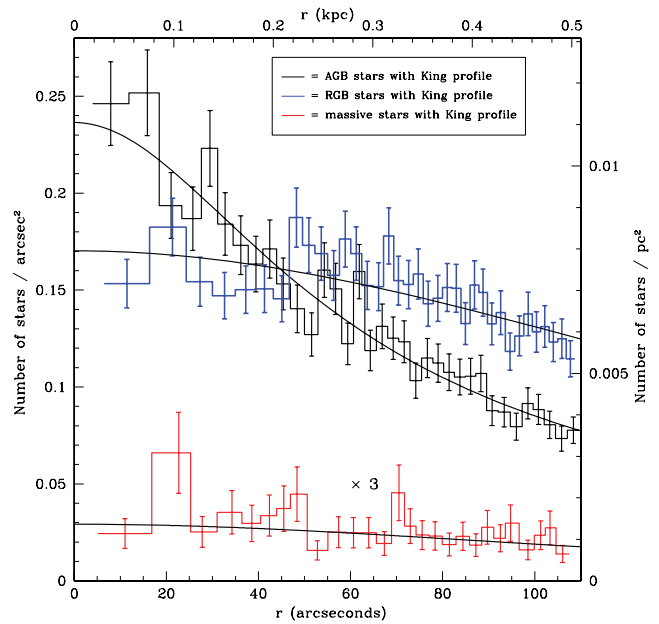

Figure 15. Radial distributions of massive stars (in red, multiplied by 3 for ease of comparison), AGB stars (in black) and RGB stars (in blue) in the image plane. Each of these is fitted with a King profile (the fit parameters are listed in Table 6).

Table 6. Fit parameters of Sérsic and King profiles for massive stars, AGB stars (Sérsic+disc) and RGB stars in the central square kpc of M33.

Sérsic profile					
Population	N_0		R_e		n
	(arcsec^{-2})	(pc^{-2})	(arcsec)	(kpc)	
Massive stars	0.0021	0.00010	199	0.92	0.67
AGB stars	0.025	0.0012	64	0.30	0.78
(exp. disc:)	0.050	0.0023	846	3.92	
RGB stars	0.042	0.0020	420	1.94	0.52
King profile					
Population	N_0		R_c		β
	(arcsec^{-2})	(pc^{-2})	(arcsec)	(kpc)	
Massive stars	0.010	0.0005	172	0.80	1
AGB stars	0.24	0.011	47	0.22	0.4
RGB stars	0.17	0.008	229	1.06	1

$b_n = 1.9992n - 0.3271$ for $0.5 < n < 10$ (Capaccioli 1989). The fit parameters are listed in Table 6.

The AGB distribution shows clear signs of a double-component profile, with the break occurring around $r \sim 0.4$ kpc, so in this case we fitted a Sérsic profile, with $R_e = 0.30$ kpc, plus a pure exponential disc profile:

$$N(r) = N_0 \exp(-r/R_e). \qquad (16)$$

This corroborates the result found by Kormendy & Kennicutt (2004) for the surface brightness profile: a Sérsic profile with $n = 1.09 \pm 0.18$ and $R_e = 0.31 \pm 0.05$ dominating the inner part with the outer part described by an exponential disc. Clearly, the AGB stars do not constitute a 'bulge', which would have had n closer to 4. Apart from the pure (rotating) disc component the nuclear part could possibly resemble a pseudo-bulge (which is a disc phenomenon and as such has n also close to 1).

The RGB population shows no strong central condensation, and a large effective radius $R_e \sim 2$ kpc. This is easy to understand as the RGB stars have had many Gyr to relax within the overall gravitational potential of the entire M33 galaxy. The massive star population too, while more centrally concentrated than the RGB population, is spread throughout the M33 disc, without a strong nuclear component. This suggests that steady star formation takes place throughout the M33 disc, with only a marginal concentration towards the nucleus. Possibly, the epochs of enhanced star formation *are* a feature of the central regions of M33, leading to the lasting imprint in the AGB stars' distribution in the form of a pseudo-bulge.

The radial distributions of stars as measured in the image plane are shown in Fig. 15. These are fitted with one of the various King models (King 1962):

$$N(r) = N_0 \left(1 + (r/R_c)^2\right)^{-(3/2)\beta}. \qquad (17)$$

The fit parameters are listed in Table 6.

Interestingly, the fits are not significantly better or worse than for the Sérsic profiles fitted in the galaxy plane. While it may seem reasonable to expect that the old RGB stars constitute a pressure-supported, more spheroidal system, the success of the Sérsic fit with a small value for n suggests that perhaps they form part of a more flattened system. In either case the RGB population has the largest characteristic radius among the three populations. The massive stars and at least a fraction of the intermediate-age AGB stars are not expected to reside in a spheroidal configuration, as they form within the gas-rich disc and will not have had time to reconfigure into a dynamically relaxed system – for these populations the Sérsic profile fits yield more plausible results.

Another way to illustrate the central condensation as a function of population age is achieved by comparing the average stellar surface density within and outside a given radius (Fig. 16; the radius is defined in the galaxy plane). This suggests that star formation has gradually become more concentrated towards the central regions, or that star formation has always been concentrated towards the core
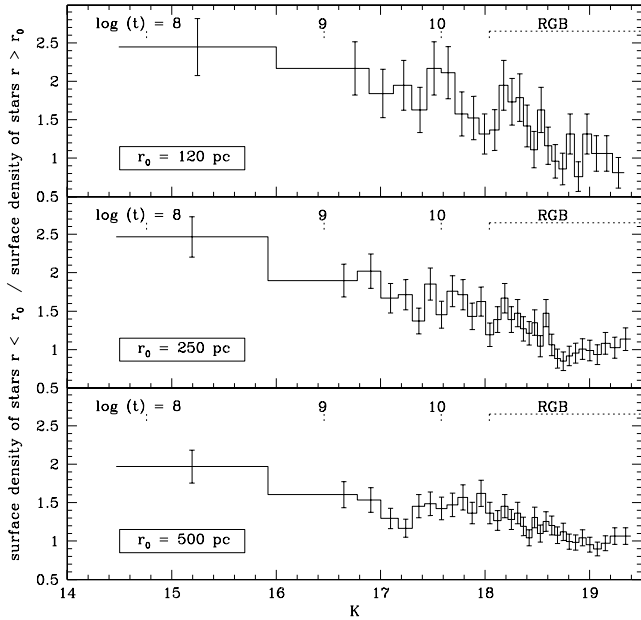
Figure 16. Ratio of stellar density inside and outside of 120 (top panel), 250 (middle panel) or 500 pc (bottom panel) for the massive stars, AGB stars and RGB stars. While the RGB populations are not centrally concentrated (a ratio near unity) the AGB and massive stellar populations are progressively more centrally concentrated the younger they are.

with dynamical relaxation having dispersed stars as time went by. We stress that we are looking here at variations within the inner square kpc, and that further out the situation might well differ.

One could wonder whether we are already noticing the gravitational potential responsible for the spiral arm pattern that so clearly defines M33. Or, would the pseudo-bulge be tri-axial, like a bar potential? In either case we would expect an azimuthal modulation with two maxima and two minima offset by an angle $\Delta\phi = \pi$. In Fig. 17 we plot these distributions for the three stellar populations, both in the image plane and in the galaxy plane. These distributions
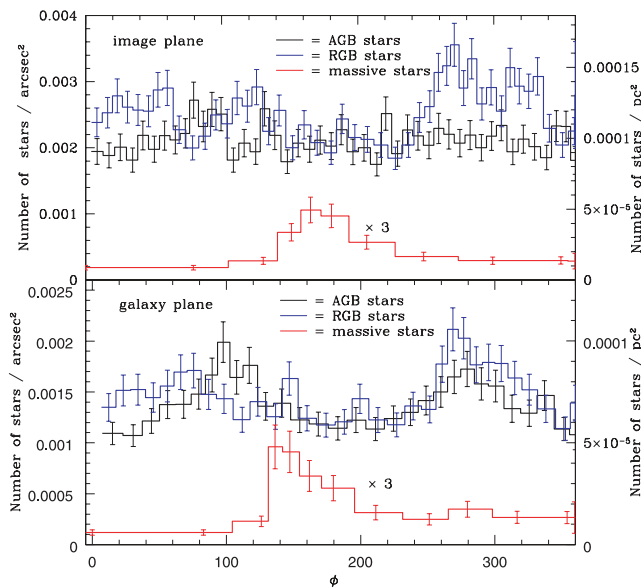

Figure 17. Azimuthal distributions of the massive stars (in red), AGB stars (in black) and RGB stars (in blue) in the image plane (top panel) and galaxy plane (bottom panel).

are constructed only for stars within circular areas in the image and galaxy planes, respectively, so as not to introduce spurious modulations due to the corners of the image resulting from the generally falling stellar surface density with distance to the galaxy centre.

The AGB population seems not to show any significant azimuthal structure in the image plane, but in the galaxy plane it does show the modulation expected from a bar or two-armed spiral arm pattern, with stellar surface density peaks around $\phi_{galaxy} \sim 100°$ and $280°$, i.e. roughly in the east and west directions. The RGB population shows a similar distribution in the galaxy plane, with an enhancement also visible in the image plane around $\phi_{image} \sim 260°–330°$, i.e. westwards. The massive stars, on the other hand, show a clear overdensity towards the south, $\phi_{image} \sim 170°$.

5 DISCUSSION AND CONCLUSIONS

The photometric catalogue of Paper I was used to reconstruct the SFH and structure of the inner square kpc of M33. The numbers and luminosities of the pulsating AGB stars and red supergiants were converted to SFRs as a function of look-back time, using recent Padova stellar evolution models (Marigo et al. 2008). Consistency checks between the predicted luminosities and pulsation durations and the derived SFRs lend strong support for these models except that the super-AGB stars must also reach high luminosities and pulsate for a considerable amount of time to avoid implausible values for the inferred SFRs. This also supports the interpretation of dust-enshrouded supernovae as being due to super-AGB star progenitors.

Our conclusions pertaining to the SFH in the centre of M33 can be summarized as follows.

(i) The disc of M33 was built ≥6 Gyr ago ($\log t \geq 9.8$), when ≥80 per cent of the historic star formation in M33 occurred.

(ii) Shorter epochs of enhanced star formation (may) have occurred since then; the most recent substantial example of such event occurred ∼250 Myr ago ($\log t \sim 8.4$) and contributed ≤6 per cent to M33's historic star formation.

(iii) A minor star formation event which had been suggested to have occurred within the nuclear star cluster within the past ∼40 Myr ($\log t \lesssim 7.6$) can also be discerned in our data suggesting this was a more widespread phenomenon.

The formation epoch of M33 around $t \geq 6$ Gyr is in line with the peak in the distribution of formation epochs of bulgeless galaxies in a standard ΛCDM cosmological model, around redshift $z \sim 1$ (Fontanot et al. 2011) corresponding to ages $t \sim 7$ Gyr. We speculate that more recent star formation epochs may have been induced by interaction with the neighbouring more massive Andromeda spiral galaxy (M31; Richardson et al. 2011).

Comparison with the historical drawing of M33 by R. J. Mitchell and published in Lord Rosse's records shows a reasonable correspondence between the footpoints of the spiral-arm pattern revealed in the unresolved white light and the density enhancements that we recorded (Fig. 18). The two main spiral arms seem to originate around $\phi_{image} \sim 90°–120°$ and $\sim 270°$ with a southern spur visible close to the centre. The spiral arms may be associated with the overdensities in AGB stars and RGB stars, though it would be somewhat coincidental that the signal in the AGB distribution is so perfectly cancelled by the projection on the sky. Furthermore, one might not have expected a signal so clear in the distribution of RGB stars, if these occupy a more spheroidal, dynamically relaxed distribution. Possibly we are dealing with a bar-like feature, which is a disc-related structure and may be connected to the footpoints of
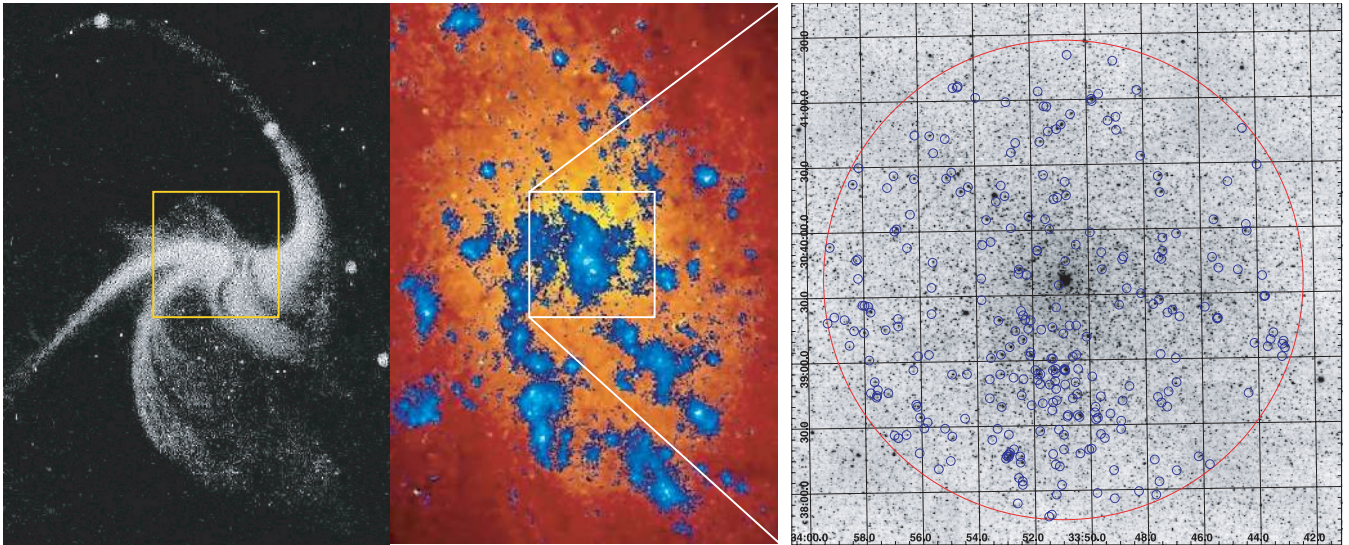
Figure 18. Left: drawing of M33 made by R. J. Mitchell (Rosse 1850). Middle: Ultraviolet Imaging Telescope image in blue, against an optical image in yellow/red (Landsman et al. 1992). Right: UFTI image of the central square kpc of M33 (the box in the left-hand panels), with overlain the massive stars (circles) and the circular area within which we constructed the azimuthal distribution in the image plane.

the spiral arms – in fact the Sérsic index $n \sim 0.5$–0.8 is smaller than that of a pure exponential disc, with galactic bars generally having $n \sim 0.5$.

The southern spur, on the other hand, can be associated with the overdensity of massive stars, which are displayed on our UFTI image (Fig. 18). This includes a prominent cluster at (RA, Dec.) $\sim$ $(1^h33^m53^s, +30°38'15'')$. The southern spur is also prominent in ultraviolet images obtained with the Ultraviolet Imaging Telescope onboard space shuttle *Columbia* (Landsman et al. 1992). Note also that the region within $\sim$30 arcsec is actually rather devoid of massive stars; this is also where the pseudo-bulge (or bar) is seen, which therefore seems to be a predominantly intermediate-age feature.

ACKNOWLEDGMENTS

REFERENCES

Asplund M., Grevesse N., Sauval A. J., Scott P., 2009, ARA&A, 47, 481
Benjamin R. A. et al., 2005, ApJ, 630, L149
Bertelli G., Bressan A., Chiosi C., Fagotto F., Nasi E., 1994, A&AS, 106, 275
Bonanos A. Z. et al., 2006, ApJ, 652, 313
Botticella M. T. et al., 2009, MNRAS, 398, 1041
Capaccioli M., 1989, in Corwin H. G., Bottinelli L., eds, The World of Galaxies. Springer-Verlag, Berlin, p. 208
Cioni M.-R. L. et al., 2008, A&A, 487, 131
Ciotti L., 1991, A&A, 249, 99
Deul E. R., van der Hulst J. M., 1987, A&AS, 67, 509
de Vaucouleurs G., 1953, MNRAS, 113, 134
Eldridge J. J., Tout C. A., 2004, Mem. Soc. Astron. Ital., 75, 694
Ferrarotti A. S., Gail H.-P., 2006, A&A, 557, 553
Fluks M. A., Plez B., Thé P. S., de Winter D., Westerlund B. E., Steenman H. C., 1994, A&AS, 105, 311
Fontanot F., De Lucia G., Wilman D., Monaco P., 2011, MNRAS, submitted (arXiv:1102.3188)
Fox M. W., Wood P. R., 1982, ApJ, 259, 198
Girardi L., Marigo P., 2007, A&A, 462, 237
Groenewegen M. A. T., 2006, A&A, 448, 181
Groenewegen M. A. T., de Jong T., 1993, A&A, 267, 410
Heger A., Woosley S. E., Spruit H. C., 2005, ApJ, 626, 350
Hodierna G. B., 1654, De Systemate Orbis Cometici, Deque Admirandis Coeli Characteribus (About the Systematics of the Cometary Orbit, and About the Admirable Objects of the Sky). Palermo
Iben I., Jr, Renzini A., 1983, ARA&A, 21, 271
Ita Y. et al., 2004a, MNRAS, 347, 720
Ita Y. et al., 2004b, MNRAS, 353, 705
Javadi A., van Loon J. Th., Mirtorabi M. T., 2011a, MNRAS, 411, 263 (Paper I)
Javadi A., van Loon J. Th., Mirtorabi M. T., 2011b, in Kerschbaum F., Lebzelter T., Wing R. F., eds, ASP Conf. Ser. Why Galaxies Care About AGB Stars II. Astron. Soc. Pac., San Francisco, preprint (arXiv:1101.5271)
King I. R., 1962, AJ, 67, 471
Kormendy J., Kennicutt R. C., Jr, 2004, ARA&A, 42, 603
Kormendy J., McClure R. D., 1993, AJ, 105, 1793
Kroupa P., 2001, MNRAS, 322, 231
Landsman W. B., Roberts M. S., Bohlin R. C., O'Connell R. W., Smith A. M., Stecher T. P., 1992, ApJ, 401, L83
Lauer T. R., Faber S. M., Ajhar E. A., Grillmair C. J., Scowen P. A., 1998, AJ, 116, 2263
Loidl R., Lançon A., Jørgensen U. G., 2001, A&A, 371, 1065
Long K. S., Charles P. A., Dubus G., 2002, ApJ, 569, 204
McDonald I., van Loon J. Th., Dupree A. K., Boyer M. L., 2010, MNRAS, 405, 1711
Magrini L., Stanghellini L., Villaver E., 2009, ApJ, 696, 729
Marigo P., Girardi L., 2007, A&A, 469, 239
Marigo P., Girardi L., Bressan A., Groenewegen M. A. T., Silva L., Granato G. L., 2008, A&A, 482, 883

Marshall J. R., van Loon J. Th., Matsuura M., Wood P. R., Zijlstra A. A., Whitelock P. A., 2004, MNRAS, 355, 1348

Massey P., Bianchi L., Hutchings J. B., Stecher T. P., 1996, ApJ, 469, 629

Messier C., 1771, Mem. Acad., 448

Meynet G., Maeder A., 2000, A&A, 361, 101

Minniti D., Olszewski E. W., Rieke M., 1993, ApJ, 410, L79

Ostlie D. A., Cox A. N., 1986, ApJ, 311, 864

Regan M. W., Vogel S. N., 1994, ApJ, 434, 536

Richardson J. C. et al., 2011, ApJ, in press (arXiv:1102.2902)

Ritossa C., García-Berro E., Iben I., Jr, 1996, ApJ, 460, 489

Rosolowsky E., Simon J. D., 2008, ApJ, 675, 1213

Rosse, Lord (Parsons W.), 1850, Philos. Trans., 499

Rowe J. F., Richer H. B., Brewer J. P., Crabtree D. R., 2005, AJ, 120, 2437

Scowcroft V., Bersier D., Mould J. R., Wood P. R., 2009, MNRAS, 396, 1287

Sérsic J. L., 1963, Bol. Asociación Argentina Astron., 6, 41

Siess L., 2007, A&A, 476, 893

Siess L., 2010, A&A, 512, A10

Stephens A. W., Frogel J. A., 2002, AJ, 124, 2023

Stetson P. B., 1993, in Butler C. J., Elliott I., eds, IAU Colloq. Ser. 136, Stellar Photometry – Current Techniques and Future Developments. Cambridge Univ. Press, Cambridge, p. 291

Stetson P. B., 1996, PASP, 108, 851

van den Bergh S., 1991, PASP, 103, 609

van Loon J. Th., Zijlstra A. A., Whitelock P. A., Waters L. B. F. M., Loup C., Trams N. R., 1997, A&A, 325, 585

van Loon J. Th., Groenewegen M. A. T., de Koter A., Trams N. R., Waters L. B. F. M., Zijlstra A. A., Whitelock P. A., Loup C., 1999, A&A, 351, 559

van Loon J. Th. et al., 2003, MNRAS, 338, 857

van Loon J. Th., Cioni M.-R. L., Zijlstra A. A., Loup C., 2005a, A&A, 438, 273

van Loon J. Th., Marshall J. R., Zijlstra A. A., 2005b, A&A, 442, 597

van Loon J. Th., Cohen M., Oliveira J. M., Matsuura M., McDonald I., Sloan G. C., Wood P. R., Zijlstra A. A., 2008, A&A, 487, 1055

Vassiliadis E., Wood P. R., 1993, ApJ, 413, 641

Ventura P., D'Antona F., 2011, MNRAS, 410, 2760

Whitelock P., Feast M., Catchpole R., 1991, MNRAS, 248, 276

Wilson C. D., Scoville N., Rice W., 1991, AJ, 101, 1293

Wood P. R., 2000, Publ. Astron. Soc. Aust., 17, 18

Zaritsky D., Elston R., Hill J. M., 1989, AJ, 97, 97

This paper has been typeset from a TEX/LATEX file prepared by the author.